



# Rheology of dense suspensions of ideally conductive particles in an electric field

Siamak Mirfendereski<sup>1</sup> and Jae Sung Park<sup>1,†</sup>

<sup>1</sup>Department of Mechanical and Materials Engineering, University of Nebraska-Lincoln, Lincoln, NE 68588-0526, USA

(Received 19 June 2023; revised 24 September 2023; accepted 15 November 2023)

The rheological behaviour of dense suspensions of ideally conductive particles in the presence of both electric field and shear flow is studied using large-scale numerical simulations. Under the action of an electric field, these particles are known to undergo dipolophoresis (DIP), which is the combination of two nonlinear electrokinetic phenomena: induced-charge electrophoresis (ICEP) and dielectrophoresis (DEP). For ideally conductive particles, ICEP is predominant over DEP, resulting in transient pairing dynamics. The shear viscosity and first and second normal stress differences  $N_1$  and  $N_2$  of such suspensions are examined over a range of volume fractions  $15\% \leq \phi \leq 50\%$  as a function of Mason number  $Mn$ , which measures the relative importance of viscous shear stress over electrokinetic-driven stress. For  $Mn < 1$  or low shear rates, the DIP is shown to dominate the dynamics, resulting in a relatively low-viscosity state. The positive  $N_1$  and negative  $N_2$  are observed at  $\phi < 30\%$ , which is similar to Brownian suspensions, while their signs are reversed at  $\phi \geq 30\%$ . For  $Mn \geq 1$ , the shear thickening starts to arise at  $\phi \geq 30\%$ , and an almost five-fold increase in viscosity occurs at  $\phi = 50\%$ . Both  $N_1$  and  $N_2$  are negative for  $Mn \gg 1$  at all volume fractions considered. We illuminate the transition in rheological behaviours from DIP to shear dominance around  $Mn = 1$  in connection to suspension microstructure and dynamics. Lastly, our findings reveal the potential use of nonlinear electrokinetics as a means of active rheology control for such suspensions.

**Key words:** suspensions, Stokesian dynamics, electrokinetic flows

## 1. Introduction

Electric-field-driven suspensions of small particles have been appreciated as a promising context for effectively manipulating the particle configuration and actively controlling the

† Email address for correspondence: [jaesung.park@unl.edu](mailto:jaesung.park@unl.edu)

stress transfer of fluids (Yeh, Seul & Shraiman 1997; Velev & Bhatt 2006; Sheng & Wen 2012; Li *et al.* 2018; Driscoll & Delmotte 2019). Playing a crucial role in the driving mechanism of such fluids, nonlinear electrokinetic phenomena have been widely exploited in a variety of fields, among which are material science, bioengineering, nanofluidics and microfluidics (Feng *et al.* 2020; Xuan 2022). In particular, a growing interest in slurry batteries containing suspended conductive particles requires a deep investigation into nonlinear electrokinetic phenomena resulting specifically from particle polarizability (Presser *et al.* 2012; Soloveichik 2015; Tan *et al.* 2019; Sánchez-Díez *et al.* 2021; Heidarian, Cheung & Rosengarten 2022). However, the current understanding of utilizing the electrokinetics for tuning the suspension rheology is mainly limited to non-conductive or weakly conductive particle systems.

For non-conductive or weakly conductive particles suspended in an insulating fluid, the classical example of nonlinear electrokinetics is dielectrophoresis (DEP), under which the particles experience dipole moments upon the application of an electric field. Resulting dipolar interactions between the particles cause them to assemble into chain/column-like structures along the field direction. Such a well-known response belongs to a popular class of smart fluids or the so-called electrorheological (ER) fluid (Wang *et al.* 2000; Sheng & Wen 2012). As a main characteristic of the typical ER fluids, the rapid formation of the field-aligned anisotropic structures under the action of an electric field induces a dramatic viscosity enhancement, potentially leading to a phase transition from a liquid to a solid state. These reversible and controllable features make the ER fluids an attractive material of choice for a variety of applications, including valves (Whittle *et al.* 1994; Choi *et al.* 1997), active shock absorbers (Choi *et al.* 2007), clutches (Madeja, Keszy & Keszy 2011) and actuators (Mazursky, Koo & Yang 2019). Furthermore, as relevant to technical applications of the ER fluids, their rheological response to an external shear flow has been extensively explored (Klingenberg, Van Swol & Zukoski 1989; Klingenberg, van Swol & Zukoski 1991; Bonnecaze & Brady 1992*a,b*; Qian, McKinley & Hosoi 2013). The rheological properties are strongly related to the response of the field-induced structures to the external flow, where the elastic body-like deformation was developed at low shear rates, while rapid transient structural arrangement occurred at high shear rates (Parthasarathy & Klingenberg 1996; Qian *et al.* 2013). Hence, such rheological behaviour of the ER fluids was primarily described by the Bingham constitutive model (Bonnecaze & Brady 1992*b*). In addition to the ER fluid, a similar rheological response can also be generated by applying a magnetic field to a suspension, which leads to a well-known concept of the so-called magnetorheological fluid (von Pfeil *et al.* 2002; De Vicente, Klingenberg & Hidalgo-Alvarez 2011; Ruiz-López *et al.* 2016).

Rheological properties of a suspension of non-conductive particles can also be modified by a completely different mechanism than the ER fluid. Upon the application of strong electric fields above the critical strength, the particles can start to undergo spontaneous sustained rotation via an effect of the so-called Quincke rotation (Quincke 1896). This effect arises primarily due to the symmetry breaking when the polarized cloud of ions around the particle induces a dipole antiparallel to the field, which is the case when the charge relaxation time of the particles is greater than that of the suspending fluid (Lobry & Lemaire 1999; Das & Saintillan 2013; Saintillan 2018; Pradillo, Karani & Vlahovska 2019; Sherman & Swan 2020). Under the Quincke instability, the particles spin around a random axis orthogonal to the field direction (Sherman & Swan 2020). When placed in an external shear flow with an electric field in the velocity-gradient direction, the rotation axis of the particles tends to align with the vorticity direction (Pannacci, Lemaire & Lobry 2007; Dolinsky & Elperin 2009; Das & Saintillan 2013). As a result, the particles spin

with an angular velocity that exceeds one of the imposed flow, leading to a reduction in the effective shear viscosity. For Quincke rotors, it was shown that increasing the field strength results in a faster particle rotation and thus a further decrease in the viscosity (Lobry & Lemaire 1999).

Until now, controlling the microstructure and macroscopic rheological properties via an external electric field has been mostly limited to the suspension of non-conductive particles whose responses to the electric field and shear flow have been well understood. A relatively new class of suspensions that contains conductive particles suspended in an electrolyte, which is the case of interest for this study, has gained a growing interest in timely applications, such as additive manufacturing (Tan *et al.* 2019) and electrochemical energy storage systems (Presser *et al.* 2012; Nikonenko *et al.* 2014; Rommerskirchen, Gendel & Wessling 2015; Soloveichik 2015; Sánchez-Díez *et al.* 2021; Folaranmi *et al.* 2022). In such suspensions, another nonlinear electrokinetic phenomenon is expected to arise with characteristics dissimilar to one typically seen in ER fluids. Under the action of the electric field  $E$ , the conductive particles can acquire an additional non-uniform charge around their surface. This charging process results in the non-uniform zeta potential distribution, which, in turn, drives a nonlinear quadrupolar flow around the particles. This flow is termed as induced-charge electroosmosis (ICEO) (Squires & Bazant 2004). The ICEO flow is easily seen by the Helmholtz–Smoluchowski equation to scale quadratically with the magnitude of the applied electric field  $E = |E|$  because the induced zeta potential or additional surface charge is solely driven by the electric field. While the ICEO flow is perfectly symmetric for a single spherical particle, symmetric breaking can arise for a suspension due to a disturbance from other particles. The broken symmetries then result in the motion of the conductive particles, which is termed as induced-charge electrophoresis (ICEP) (Squires & Bazant 2004, 2006). This nonlinear electrokinetic phenomenon was first described by Murtsovkin and coworkers (Dukhin & Murtsovkin 1986; Gamayunov, Murtsovkin & Dukhin 1986; Murtsovkin 1996). Unlike the ER fluid, the particles undergoing ICEP show transient pairing dynamics, where they tend to approach along the field direction, pair up and eventually separate in the transverse directions (Saintillan 2008). It is important to point out that when the suspension of conductive particles is placed in an external electric field, the particle motions arise undergoing both ICEP and DEP concurrently, which is sometimes referred to as dipolophoresis (DIP) (Shilov & Simonova 1981). Nevertheless, it was found that DIP is mainly governed by ICEP for ideally conductive particles in a low-frequency field because of the slower decay of ICEP interactions as  $O(R^{-2})$  with separation distance  $R$  compared with  $O(R^{-4})$  for DEP interactions (Saintillan 2008; Park & Saintillan 2010; Kilic & Bazant 2011).

For zero-shear-limiting suspensions, we found that DIP exhibits intriguing non-trivial behaviours at the concentrated regime around a volume fraction  $\phi$  in a range of  $35\% \leq \phi \leq 50\%$  (Mirfendereski & Park 2019, 2021). More specifically, the hydrodynamic diffusivity and particle velocity fluctuation start to increase at  $\phi \approx 35\%$  despite the expectation that they should continue to decrease with increasing  $\phi$  due to the increase in the magnitude of excluded volume interactions (Mirfendereski & Park 2019). They then reach a local maximum at  $\phi \approx 45\%$  before decreasing again towards zero as  $\phi$  approaches random close packing. Interestingly, such non-trivial dynamics was associated with the onset of negative particle pressure at  $\phi \approx 30\%$ , which eventually becomes maximum at  $\phi \approx 45\%$  (Mirfendereski & Park 2021). A mechanism for these counter-intuitive behaviours was explained by the transition in the dominant mechanism of particle pairing arising at the concentrated regime. For a dilute DIP suspension, the particle pairing is mostly dominated by attractive particle contacts along the field direction, and contact

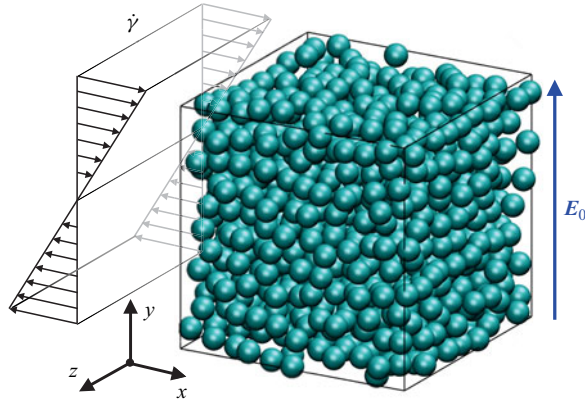


Figure 1. A suspension of ideally conductive spheres under an external shear flow with constant shear rate  $\dot{\gamma}$  and a uniform electric field  $E_0$ . Note that the direction of the applied electric field is set to align with the velocity-gradient direction of the external shear flow, which is orthogonal to the flow direction.

motions are relatively slow. For semidilute and dense DIP suspensions, however, there are massive, very strong and fast repulsive particle contacts in the direction perpendicular to an electric field, which is believed to be a driving mechanism for the non-trivial behaviours (Mirfendereski & Park 2019).

While it has been focused mainly on the zero-shear-rate limit for DIP, not much effort has been made to determine the shear rheology of suspensions undergoing DIP, for which the present work aims at providing the first insight. In this paper, we develop and use large-scale numerical simulations to explore the rheology of dense suspensions of non-colloidal conductive particles undergoing both DIP and shear flow. The current simulation model is based on the Stokesian dynamics technique incorporating the mobility-based methodology for DIP (Saintillan, Darve & Shaqfeh 2005; Mirfendereski & Park 2019) and the resistance-based methodology for shear flow (Bossis & Brady 1984; Durlofsky, Brady & Bossis 1987; Brady & Bossis 1988). In § 2, the simulation model is described in more detail. We provide the simulation results in § 3, where we present the shear viscosity and normal stress differences of the suspension followed by suspension microstructure and dynamics. We then conclude in § 4.

## 2. Governing equations and simulation method

We consider a suspension of  $N$  identical neutrally buoyant spheres of radius  $a$  in a viscous electrolyte with permittivity  $\varepsilon$  and viscosity  $\eta$ . The spheres are considered smooth, ideally conductive or polarizable, and sufficiently large so that the Brownian motion is negligible. As demonstrated in figure 1, the suspension experiences a uniform electric field  $\mathbf{E}_0 = E_0 \hat{y}$  and simple shear flow  $\mathbf{u}^\infty = \mathbf{K}^\infty \cdot \mathbf{x}$ , simultaneously, where the  $x$ ,  $y$  and  $z$  axes represent the flow, velocity-gradient and vorticity directions of the external shear flow, respectively. Note that the electric field is along with the velocity-gradient direction and orthogonal to the flow direction. The velocity gradient tensor  $\mathbf{K}^\infty$  of the shear flow can be given by

$$\mathbf{K}^\infty = \begin{bmatrix} 0 & \dot{\gamma} & 0 \\ 0 & 0 & 0 \\ 0 & 0 & 0 \end{bmatrix}, \quad (2.1)$$

where the shear rate  $\dot{\gamma}$  is constant for a steady shear flow. We use a cubic periodic domain of a Lees–Edwards kind (Lees & Edwards 1972) to accommodate the bulk shear flow for the simulation of an unbounded infinite suspension.

The particles are assumed to carry no net charge, so linear electrophoresis is not expected to occur under the applied electric field. We also assume weak electric fields, thin Debye layers and zero Dukhin number for no surface conduction (Squires & Bazant 2004). Under these conditions and assumptions, the applied electric field drives the relative motion of the particles entirely through DIP, which is the combination of ICEP and DEP (Saintillan 2008; Park & Saintillan 2010). For ICEP, it is important to note that the charging time of the Debye layer is very fast, of the order of  $\tau_c = \lambda_D a / D$ , where  $\lambda_D$  is the Debye layer thickness, and  $D$  is the characteristic diffusivity of ions in solution. For instance, the charging time  $\tau_c \sim 10^{-4}$  s in a typical experiment ( $a = 10 \mu\text{m}$ ,  $\lambda_D = 10 \text{ nm}$ ,  $D \sim 10^{-5} \text{ cm}^2 \text{ s}^{-1}$ ). Therefore, with the reasonable assumption of  $\tau_c \ll \dot{\gamma}^{-1}$ , we can easily ignore the distortion of the equilibrium charge cloud due to shear-induced rotation/translation of spheres and any consequent effects or potential instabilities (Khair & Balu 2019). In other words, while the particles undergo shear-induced rotation, the surface charge distribution and the screening charge cloud remain intact with respect to the external electric field.

The current simulation model captures the contributions of both DIP and shear flow to the particle motion and suspension rheology, which are detailed as follows.

### 2.1. Electrokinetics contribution

For computing the electric and hydrodynamic interactions resulting from both ICEP and DEP (i.e. DIP), we employ the method used in our previous studies (Park & Saintillan 2010, 2011b; Mirfendereski & Park 2019, 2021). Based on pair interactions calculated by Saintillan (2008) for a suspension undergoing DIP, the translational velocity of a given particle  $\alpha$  driven by ICEP and DEP under an electric field  $\mathbf{E}_0 = E_0 \hat{\mathbf{y}}$  can be expressed as

$$\mathbf{U}_\alpha^d = \frac{\varepsilon a E_0^2}{\eta} \sum_{\beta=1}^N [\mathbf{M}^{DEP}(\mathbf{R}_{\alpha\beta}/a) + \mathbf{M}^{ICEP}(\mathbf{R}_{\alpha\beta}/a)] : \widehat{\mathbf{y}}\widehat{\mathbf{y}}, \quad \alpha = 1, \dots, N, \quad (2.2)$$

where  $\mathbf{R}_{\alpha\beta} = \mathbf{x}_\beta - \mathbf{x}_\alpha$  is the separation vector between the particle  $\alpha$  and particle  $\beta$ , and  $\mathbf{M}^{DEP}$  and  $\mathbf{M}^{ICEP}$  are third-order dimensionless tensors accounting for the DEP and ICEP interactions, respectively. It is shown that these two tensors are entirely determined by the scalar functions of the dimensionless inverse separation distance  $\lambda = 2a/|\mathbf{R}|$ . For far-field interactions ( $\lambda \ll 1$ ), the DEP and ICEP far-field interaction tensors can be computed using the method of reflections and expressed up to order  $O(\lambda^4)$  in terms of two fundamental solutions of Stokes equations  $\mathbf{S}$  and  $\mathbf{T} = \nabla^2 \mathbf{S}$ , which are the Green's functions for a Stokes dipole and for a potential quadrupole, respectively (Kim & Karrila 2013). The far-field expressions of these tensors are written as follows:

$$\mathbf{M}_{FF}^{DEP} = \frac{1}{12} \mathbf{T} + O(\lambda^5), \quad (2.3)$$

$$\mathbf{M}_{FF}^{ICEP} = -\frac{9}{8} \mathbf{S} - \frac{11}{24} \mathbf{T} + O(\lambda^5). \quad (2.4)$$

These tensors can be expressed as the periodic version of the far-field tensors to account for far-field interactions between particles  $\alpha$  and  $\beta$  and all its periodic images, which are valid to order  $O(\mathbf{R}_{\alpha\beta}^{-4})$ . Direct calculation of the sums for  $\mathbf{U}_\alpha^d$  in (2.2) requires  $O(N^2)$

of computation for which the smooth particle mesh Ewald algorithm, which shares similarities to the accelerated Stokesian dynamics simulation (Sierou & Brady 2001), is used to accelerate the calculation of the sums to  $O(N \log N)$  operations (Mirfendereski & Park 2019). However, the near-field corrections are necessary as the method of reflections becomes inaccurate when the particles are close to each other (typically for  $|\mathbf{R}_{\alpha\beta}| < 4a$ ). This is achieved by correcting the far-field tensor with the more accurate method of twin multiple expansions (Saintillan 2008). This method is very accurate down to separation distances of the order of  $|\mathbf{R}_{\alpha\beta}| \approx 2.005a$ .

For DEP and ICEP interactions due to (2.3) and (2.4), it is worth noting that while both ICEP and DEP lead to similar particle pairing in the electric-field direction, the subsequent pairing dynamics is significantly different (Saintillan 2008; Park & Saintillan 2010). Specifically, ICEP leads to transient pairing dynamics, where particles briefly pair up in the field direction but then reorient themselves to align in the transverse directions, eventually leading to their separation. Such pairing dynamics give rise to chaotic collective motion. Conversely, in the DEP case, the formed pairs remain in a stable equilibrium, ultimately resulting in the formation of stable chains/columns along the field direction. In the case of DIP, when both ICEP and DEP coexist, transient pairing dynamics only occur due to the predominance of ICEP over DEP, as can be alluded to by the leading orders of the ICEP and DEP interactions, which are a Stokes dipole of  $O(\lambda^2)$  and a potential quadrupole of  $O(\lambda^4)$ , respectively.

### 2.2. Shear flow contribution

The contribution of the external shear flow  $\mathbf{u}^\infty$  to the particle motion and bulk stress is calculated by the classical resistance-based Stokesian dynamics approach (Brady & Bossis 1988). Owing to the linearity of the Stokes equation, we can relate the moments of the hydrodynamic force density on the particle surfaces to the relative velocity moments of particles by the grand resistance tensor  $\mathcal{R}$  as given by

$$\begin{bmatrix} \mathbf{F} \\ \mathbf{T} \\ \mathbf{S} \end{bmatrix} = -\mathcal{R} \cdot \begin{bmatrix} \mathbf{U} - \mathbf{u}^\infty \\ \boldsymbol{\Omega} - \boldsymbol{\omega}^\infty \\ -\mathbf{E}^\infty \end{bmatrix}, \quad (2.5)$$

where  $\mathbf{U}$  and  $\boldsymbol{\Omega}$  are translational and rotational velocities of particles, respectively, and  $\mathbf{F}$ ,  $\mathbf{T}$  and  $\mathbf{S}$  are the force, torque, and stresslet on particles, respectively. The rate of strain  $\mathbf{E}^\infty$  is the symmetric part of  $\mathbf{K}^\infty$ , and  $\boldsymbol{\omega}^\infty = 1/2\nabla \times \mathbf{u}^\infty$  gives the vorticity of the imposed flow. The grand resistance tensor  $\mathcal{R}$  can be approximated as a sum of the Stokes drag and the pairwise lubrication interactions since the dominant hydrodynamic interactions come from the pairwise short-range lubrication forces for dense suspensions (Mari *et al.* 2014). The grand resistance tensor  $\mathcal{R}$  can be then written by the combination of the resistance matrices (Bossis & Brady 1987),

$$\mathcal{R} = \begin{bmatrix} \mathbf{R}_{FU} & \mathbf{R}_{FE} \\ \mathbf{R}_{SU} & \mathbf{R}_{SE} \end{bmatrix}, \quad (2.6)$$

where the  $6N \times 6N$  second-rank tensor  $\mathbf{R}_{FU}$  relates the hydrodynamic forces/torques on particles to their motion (translation/rotational velocity) relative to the imposed flow. The third-rank tensors  $\mathbf{R}_{FE}$  and  $\mathbf{R}_{SU}$  relate the hydrodynamic forces/torques to the rate of strain and the particle stresslet to the relative motion of particles, respectively. The fourth-rank tensor  $\mathbf{R}_{SE}$  gives the particle stresslet owing to the rate of strain. These resistance tensors are configuration-dependent, and their elements can be expressed by the relationships

between the unit vector along the centreline of each pair of particles  $\hat{\mathbf{R}} = \mathbf{R}_{\alpha\beta}/|\mathbf{R}_{\alpha\beta}|$  and the scalar resistance functions of  $\lambda$ . The details of calculating these resistance tensors were provided by Jeffrey & Onishi (1984), Kim & Mifflin (1985), Jeffrey (1992) and Kim & Karrila (2013).

### 2.3. Total particle velocity

We calculate the total particle velocity and stress by superposing the contributions of DIP and shear flow thanks to the linearity of the Stokes equation. Hence, the total translational velocity  $\mathbf{U}^t$  and rotational velocity  $\boldsymbol{\Omega}^t$  of the particles are given by

$$\begin{bmatrix} \mathbf{U}^t \\ \boldsymbol{\Omega}^t \end{bmatrix} = \begin{bmatrix} \mathbf{u}^\infty \\ \boldsymbol{\omega}^\infty \end{bmatrix} + \mathbf{R}_{FU}^{-1} \cdot \mathbf{R}_{FE} : \mathbf{E}^\infty + \mathbf{R}_{FU}^{-1} \cdot \mathbf{F}^p + \begin{bmatrix} \mathbf{U}^d \\ \boldsymbol{\Omega}^d \end{bmatrix}, \quad (2.7)$$

where  $\boldsymbol{\Omega}^d = \mathbf{0}$  as no particle rotation arises as a result of DIP for the perfectly symmetric spheres (Saintillan 2008). The explicit calculation of the second and third terms on the right-hand side of (2.7) is prohibitively expensive due to an inversion of the resistance tensor  $\mathbf{R}_{FU}$ , which is of an order of  $O(N^3)$ . For the sake of fast calculations, we use the generalized minimal residual method (Saad & Schultz 1986) to resolve these terms. The interparticle force  $\mathbf{F}^p$  in (2.7) is written as a pairwise electrostatic repulsive force between the particles  $\alpha$  and  $\beta$  (Bossis & Brady 1984; Sierou & Brady 2002),

$$\mathbf{F}_{\alpha\beta}^p = \frac{F_0}{\sigma} \frac{e^{-\epsilon/\sigma}}{1 - e^{-\epsilon/\sigma}} \hat{\mathbf{R}}_{\alpha\beta}, \quad (2.8)$$

where  $F_0$ ,  $\sigma$  and  $\epsilon$  are the force magnitude, force range and the dimensionless spacing between the surface of particles  $\epsilon = R/a - 2$ , respectively. The magnitude of the interparticle force relative to the shear force can be controlled by the dimensionless number  $\dot{\gamma}^* = 6\pi\eta a^2 \dot{\gamma}/F_0$ . For all present simulations, the fixed values of  $\dot{\gamma}^* = 5000$  and  $\sigma = 0.001$  are employed as validated and used by Sierou & Brady (2002). It is important to note that the choice of these values for the repulsive force corresponds to a very short time scale with a negligible impact for the system studied.

Once the particle velocities are calculated by (2.7), the particle positions are advanced in time using a second-order Adams–Bashforth time-marching scheme, with an explicit Euler scheme for the first time step. A fixed time step  $\Delta t$  is chosen so as to ensure that the particles only travel a very small fraction ( $< 0.4\%$ ) of the mean interparticle distance at each iteration. However, due to the use of a finite time step, the particle overlap should be prevented, for which we employ the potential-free algorithm (Melrose & Heyes 1993) from our previous works (Mirfendereski & Park 2019, 2021). The initial random equilibrium configurations were generated using an approach similar to the one employed in our previous works (Mirfendereski & Park 2019, 2021). This method is based on the procedure suggested for dense hard-sphere systems (Stillinger, DiMarzio & Kornegay 1964; Clarke & Wiley 1987; Rintoul & Torquato 1996).

### 2.4. Bulk stress

The bulk rheological properties can be determined from the average stress tensor  $\langle \boldsymbol{\Sigma} \rangle$  (Batchelor 1970), where the angle bracket denotes the ensemble average over all particles.

The stress tensor is expressed as

$$\langle \boldsymbol{\Sigma} \rangle = -p_f \mathbf{I} + 2\eta \mathbf{E}^\infty + \langle \boldsymbol{\Sigma}^p \rangle, \quad (2.9)$$

where  $p_f$  is the average pressure in the fluid phase,  $\mathbf{I}$  is the identity matrix, and  $2\eta \mathbf{E}^\infty$  is the deviatoric contribution from the incompressible fluid. The total contribution of particle phase to the stress or particle stress  $\langle \boldsymbol{\Sigma}^p \rangle$  is given by

$$\langle \boldsymbol{\Sigma}^p \rangle = -n \left\langle \mathbf{R}_{SU} \cdot \begin{bmatrix} \mathbf{U} - \mathbf{u}^\infty \\ \boldsymbol{\Omega} - \boldsymbol{\omega}^\infty \end{bmatrix} \right\rangle + n \langle \mathbf{R}_{SE} : \mathbf{E}^\infty \rangle + n \langle \mathbf{S}^d \rangle - n \langle \mathbf{x} \mathbf{F}^p \rangle, \quad (2.10)$$

where  $n$  is the particle number density. The first and second terms in (2.10) are the hydrodynamic stresslets that come from the external shear flow (Sierou & Brady 2002; Mari *et al.* 2014), while the third term  $\langle \mathbf{S}^d \rangle$  stems from the DIP contribution (Mirfendereski & Park 2021). Note that the contribution of DEP to the stress is negligible compared with the ICEP contribution for ideally conductive particles (Mirfendereski & Park 2021). The direct interparticle force contribution is given by  $-\langle \mathbf{x} \mathbf{F}^p \rangle$  in (2.10), which is found to be negligible here.

Once the average bulk stress tensor is obtained, its  $xy$  component  $\langle \Sigma_{xy} \rangle$  is used to calculate the relative shear viscosity:

$$\eta_r = \frac{\langle \Sigma_{xy} \rangle}{2\eta E_{xy}^\infty}. \quad (2.11)$$

The normal components of the average bulk stress are also used to calculate the first and second normal stress differences:

$$N_1 = \langle \Sigma_{xx} \rangle - \langle \Sigma_{yy} \rangle, \quad (2.12)$$

$$N_2 = \langle \Sigma_{yy} \rangle - \langle \Sigma_{zz} \rangle. \quad (2.13)$$

For testing the code for validation purposes, the relative shear viscosity in the absence of an electric field is calculated using the present simulation model, which is shown in figure 2(a). In addition to the current simulation results, the experimental results by Dbouk *et al.* (2013), Denn *et al.* (2018) and Lewis & Nielsen (1968), and computational results by Sierou & Brady (2002) are present along with the Maron–Pierce correlation  $\eta_r = (1 - \phi/\phi_m)^{-2}$  with  $\phi_m = 63\%$ . A good agreement between the current and previous results is observed. In particular, the current simulation model reproduces the Maron–Pierce correlation well.

To indicate the relative importance of the viscous stress from shear flow over the electrokinetics-driven stress from DIP, the so-called Mason number ( $Mn$ ) can be used and given by

$$Mn = \frac{\eta \dot{\gamma}}{\varepsilon E_0^2}, \quad (2.14)$$

where the viscous shear stress and DIP stress scale as  $\eta \dot{\gamma}$  and  $\varepsilon E_0^2$ , respectively.

To further validate the simulation code in the presence of both electric field and shear flow, we conducted simulations for suspensions undergoing shear flow and DEP, where ICEP is absent, a scenario closely resembling typical ER fluids. Figure 2(b) illustrates the relative shear viscosity as a function of the Mason number, presenting the current simulation results along with the experimental data reported by Marshall *et al.* (1989) for ER fluids. A good agreement between the current computational results and the previous experimental data is observed.



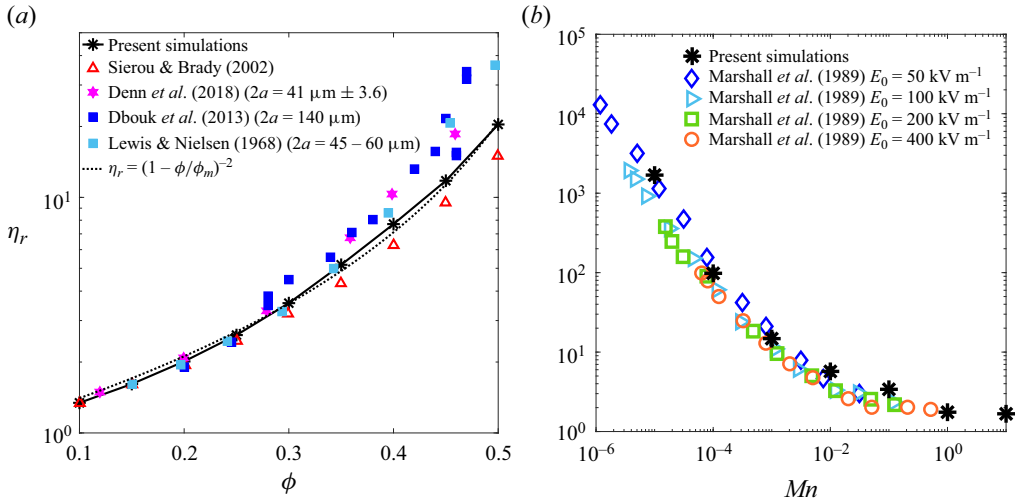


Figure 2. (a) The relative shear viscosity  $\eta_r$  of a non-Brownian suspension solely undergoing shear flow as a function of volume fraction. Also shown are the experimental results of Lewis & Nielsen (1968), Dbouk, Lobry & Lemaire (2013) and Denn, Morris & Bonn (2018), and the numerical results of Sierou & Brady (2002). The current results agree well with the numerical and experimental data reported in the literature. The dotted line is the Maron–Pierce correlation with  $\phi_m = 0.63$ . (b) Relative shear viscosity of the suspension undergoing DEP and shear flow as a function of  $Mn$  at  $\phi = 15\%$  from the current simulations. Also shown are the experimental results of Marshall, Zukoski & Goodwin (1989) for ER suspensions containing hydrated poly(methacrylate) particles in a chlorinated hydrocarbon subjected to different electric field strengths at  $\phi = 13\%$ .

### 3. Results and discussion

We performed large-scale simulations of ideally conductive particle suspensions under both electric field and shear flow in a periodic cubic domain of a Lees–Edwards kind in ranges of volume fractions and Mason numbers. The dependence on the system size was examined, confirming that the simulation results are insensitive to the domain size and the number of particles. It is worth noting again that the Mason number is the ratio of viscous shear stress and electrokinetics-driven stress, representing the dimensionless shear rate for the system studied here. However, it can also be regarded that given the shear rate, the Mason number represents the inverse of the squared dimensionless field strength. All simulation runs were initiated from the hard-sphere equilibrium configurations, and the time steps within the first 10–30 strains were discarded for statistical averaging over the steady-state configurations. To reach 200 strains  $\gamma$ , the current simulation at  $\phi = 15\%$  requires approximately 50 h of central processing unit (CPU) time, and a higher volume fraction at  $\phi = 50\%$  requires approximately seven times more CPU time as compared with  $\phi = 15\%$ . In addition, it is worth noting that the CPU time increased with higher volume fractions and lower Mason numbers. The statistical variation of the suspension properties over the steady state is determined by their standard deviation and represented by the error bar in the figures.

#### 3.1. Relative shear viscosity

We start by exploring the effects of the Mason number and volume fraction on the shear viscosity of suspensions. Figure 3(a) presents the relative shear viscosity  $\eta_r$  as a function of volume fraction for a range of Mason numbers. As seen in the figure, the high-shear-rate viscosities ( $Mn \geq 5$ ) collapse almost onto a single curve. Note that  $Mn = \infty$  refers to

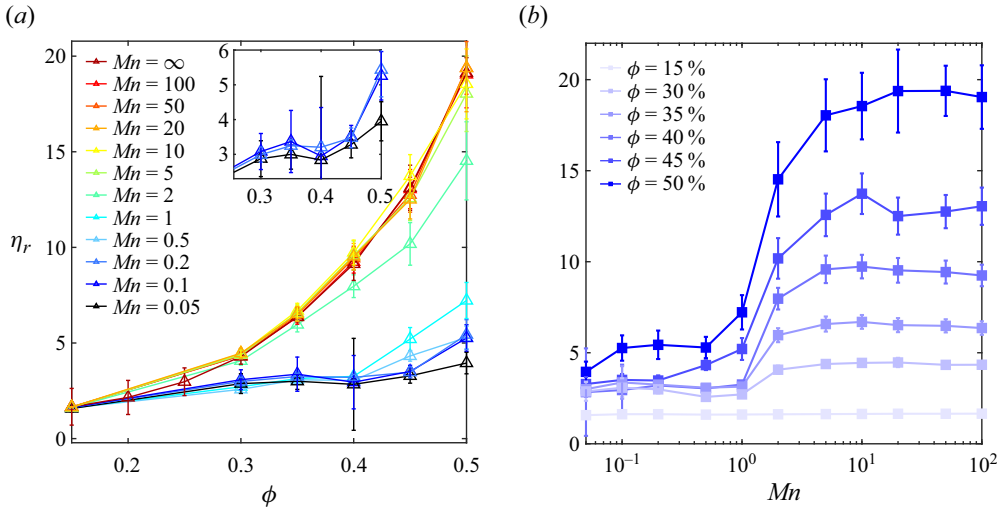


Figure 3. (a) The relative shear viscosity  $\eta_r$  of the non-Brownian suspensions undergoing both DIP and steady shear flow as a function of volume fraction for a range of Mason numbers. Note that the  $Mn = \infty$  limit refers to the viscosity in the absence of an electric field. Inset: the magnified view of the low- $Mn$  or low-shear-rate viscosities ( $Mn = 0.05, 0.1, 0.2$ ), showing a non-monotonic variation with volume fraction. (b) The relative shear viscosity is replotted as a function of Mason number for various volume fractions.

a measurement in the absence of an electric field. By reducing the shear rate or the Mason number below  $Mn = 5$ , the viscosity starts to decrease, more significantly at high volume fractions for  $\phi \geq 40\%$ . Interestingly, there is a significant decrease from  $Mn = 2$  to  $Mn = 1$ , suggesting a possible transition taking place around these Mason numbers. At the low-shear-rate regime ( $Mn < 0.5$ ), the viscosity seems to collapse again onto a single curve with smaller values than for the high-shear-rate regime. The inset of the figure shows a magnified view of the low-shear-rate viscosities ( $Mn = 0.2, 0.1, 0.05$ ) as a function of volume fraction. Interestingly, a non-monotonic variation with volume fraction is observed. These low-shear-rate viscosities start to increase with volume fraction, reach a local maximum at  $\phi \approx 35\%$  and then slightly decrease up to  $\phi \approx 40\%$  before increasing again as volume fraction is further increased. Such non-monotonic behaviour is attributed to the predominant ICEP effect over shear flow at low Mason numbers or low shear rates. This non-monotonic trend can be explained by quiescent DIP suspensions in our previous studies, where the hydrodynamic diffusivity exhibits the exact opposite trend to the shear viscosity (Mirfendereski & Park 2019) and the particle pressure exhibits a very similar non-monotonic trend (Mirfendereski & Park 2021).

To characterize a shear-dependence behaviour, the relative shear viscosity is replotted as a function of the Mason number for various volume fractions, as seen in figure 3(b). At a volume fraction as small as  $\phi = 15\%$ , the variation of viscosity with Mason number is almost negligible, indicating a Newtonian-fluid-like behaviour. For  $\phi \geq 30\%$ , however, the shear-thickening behaviour is observed. The viscosity appears to remain constant at low Mason numbers and starts to sharply increase around  $Mn = 1$ , reaching a plateau as the Mason number is further increased. Similar to figure 3(a), a significant transition again seems to occur at  $Mn \approx 1$ , which can be thus referred to as the transitional or critical Mason number for the current study. The shear thickening becomes more prominent with increasing volume fraction. At  $\phi = 45\% - 50\%$ , a large increase in viscosity occurs during the shear-thickening process, which is approximately five-fold. The underlying mechanism

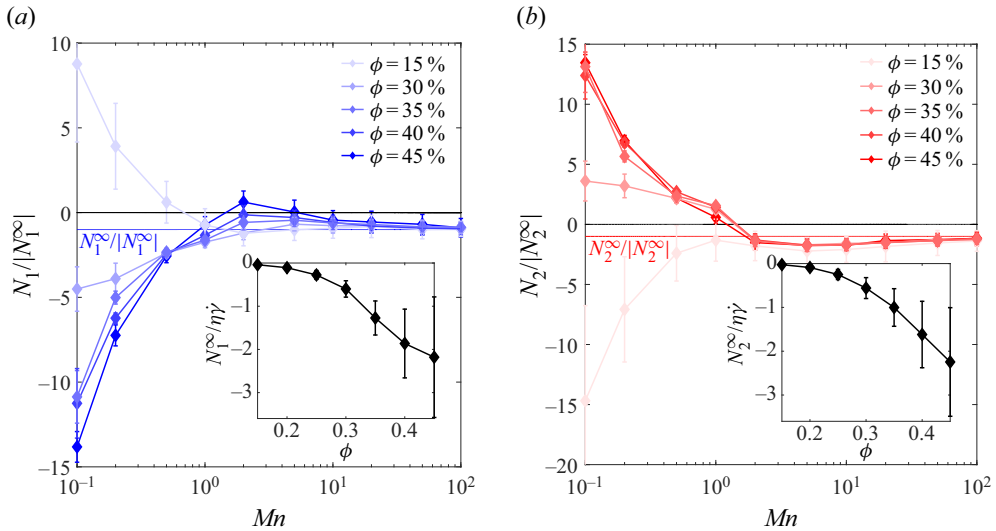


Figure 4. The (a) first and (b) second normal stress differences, normalized by their magnitude for the pure-shear-flow limit ( $Mn = \infty$ ), as a function of Mason number for various volume fractions. The insets of (a) and (b) show the first and second normal stress differences for  $Mn = \infty$  as a function of volume fraction, respectively.

of such shear thickening in the concentrated regime is intimately linked to the emergence of a distinct microstructure, which we will discuss in § 3.3. As an interesting future work, this  $Mn$ -dependent behaviour suggests a possible rheology control for a suspension of ideally conductive particles in an electric field. For example, at a given high volume fraction (i.e.  $\phi \geq 30\%$ ) and high shear rate (i.e.  $Mn > 1$ ), having stronger DIP or ICEP effects via increasing the electric-field strength could lead to a viscosity reduction from the shear-thickened states to the Newtonian-like low viscosity states.

It is interesting to note that the shear-thickening behaviour of the current DIP suspension is in contrast to what has been typically observed for the classical ER fluid, which mainly exhibits shear-thinning behaviour (Bonnecaze & Brady 1992a; Parthasarathy & Klingenberg 1996). This distinct difference in shear-dependent rheological responses should be associated with the predominance of ICEP over DEP in the DIP suspension of ideally conductive particles (Park & Saintillan 2010, 2011b). Note that the underlying mechanism of the ER fluid ties closely to DEP interactions (Mirfendereski & Park 2022).

### 3.2. Normal stress differences

As it has been observed that significant particle normal stresses are generated by DIP even at zero shear rate (Mirfendereski & Park 2021), we investigate the normal stress differences as a result of shear flow. The first and second normal stress differences, which are defined by  $N_1 = \Sigma_{xx} - \Sigma_{yy}$  and  $N_2 = \Sigma_{yy} - \Sigma_{zz}$ , respectively (Zarraga, Hill & Leighton 2000; Sierou & Brady 2002; Dbouk *et al.* 2013), are examined. Prior to proceeding to a detailed analysis for DIP suspensions with shear flow, the insets of figures 4(a) and 4(b) present the pure-shear-flow limiting normal stress differences  $N_1^\infty$  and  $N_2^\infty$  as a function of volume fraction, respectively. As clearly seen, both  $N_1^\infty$  and  $N_2^\infty$  remain negative, and their magnitude increases with volume fraction, which has also been reported both experimentally and numerically for sheared, non-colloidal suspensions (Sierou & Brady 2002; Dai *et al.* 2013; Pan *et al.* 2015; Guazzelli & Pouliquen 2018). It is worth noting that

$N_1^\infty$  and  $N_2^\infty$  at  $\phi = 45\%$  are almost the same as those for high-shear colloidal dispersions (Foss & Brady 2000) and high-shear non-colloidal dispersions (Sierou & Brady 2002). The notable error bars are observed at high volume fractions. These errors are attributed to the sensitivity of the normal stress differences to even small errors in the calculation of the average value of each normal stress component, which is also seen and explained by Sierou & Brady (2002).

Figures 4(a) and 4(b) show  $N_1$  and  $N_2$  as a function of Mason number for various volume fractions, respectively, where the normal stress differences are normalized by their values for a pure shear flow ( $Mn = \infty$ ). At low Mason numbers or specifically below the critical Mason number ( $Mn = 1$ ), the DIP effect is expected to be strong relative to the shear flow. In this DIP-dominant regime,  $N_1$  is positive for a volume fraction as small as  $\phi = 15\%$  but negative at  $\phi \geq 30\%$ . As opposed to the first normal stress difference,  $N_2$  is negative at  $\phi = 15\%$  but positive at  $\phi \geq 30\%$ . The positive  $N_1$  and negative  $N_2$  at a low volume fraction of  $\phi = 15\%$  indeed share similarities with the Brownian contributions to the normal stress differences observed in a hard-sphere colloidal dispersion (Foss & Brady 2000). The distinctive characteristics of the low-shear-rate  $N_1$  and  $N_2$  can also be explained by our previous observation of the DIP-driven normal stresses at zero shear rate (Mirfendereski & Park 2021). We observed that under DIP only, the magnitude of the normal stress in the field direction is larger than the transverse ones (i.e.  $|\Sigma_{yy}| > |\Sigma_{xx}|, |\Sigma_{zz}|$ ) for all volume fractions. In addition, the signs of field and transverse normal stresses are opposite at different regimes of volume fraction; specifically, the suspension at  $\phi < 30\%$  exhibits positive transverse normal stresses ( $\Sigma_{xx}, \Sigma_{zz}$ ) and a negative field normal stress ( $\Sigma_{yy}$ ), while the former becomes negative and the latter becomes positive at  $30\% \leq \phi \leq 50\%$ . That is again consistent with the unique low-shear-rate characteristics of  $N_1$  and  $N_2$  described above and shown in figure 4. For  $Mn \gg 1$  or well above the critical Mason number, both  $N_1$  and  $N_2$  become negative for all volume fractions considered, which indicates that the effect of shear flow becomes dominant over the DIP effect. Both  $N_1$  and  $N_2$  appear to reach a high-shear plateau for  $Mn > 10$ . It should be noted that the negative sign of both normal stress differences at high Mason numbers is well observed in concentrated suspensions, especially in the shear-thickened states (Cwalina & Wagner 2014).

### 3.3. Suspension microstructure

As the suspension microstructure has been regarded as a microscopic basis of the shear viscosity and the normal stress differences (Wagner & Ackerson 1992; Brady & Morris 1997; Zarraga *et al.* 2000), we attempt to investigate the microstructural variation in connection to the variation of the macroscopic rheological properties. To directly characterize the microstructure undergoing both DIP and shear flow, we calculate the pair distribution function (Park & Saintillan 2010; Mirfendereski & Park 2019). This function provides the probability of finding the particles with respect to a reference particle placed at the origin. Figure 5 shows the projection of this function on the shear plane ( $x$ - $y$ ) for various Mason numbers at volume fractions of  $\phi = 15\%$ ,  $30\%$  and  $45\%$ . At  $Mn = 0.1$ , which is below the critical Mason number, the function is symmetric with respect to the  $y$  axis (the electric-field direction) for all volume fractions considered. However, it is interesting to note that as the volume fraction increases, the location of the maximum probability changes from near the particle poles ( $\phi = 15\%$ ) to the particle equators ( $\phi = 30\%, 45\%$ ), which is similar to the zero-shear-rate limiting suspension (Mirfendereski & Park 2019, 2021). On the relation of the microstructure to the normal stress differences, the high probability near the poles formed at  $\phi = 15\%$  and  $Mn = 0.1$

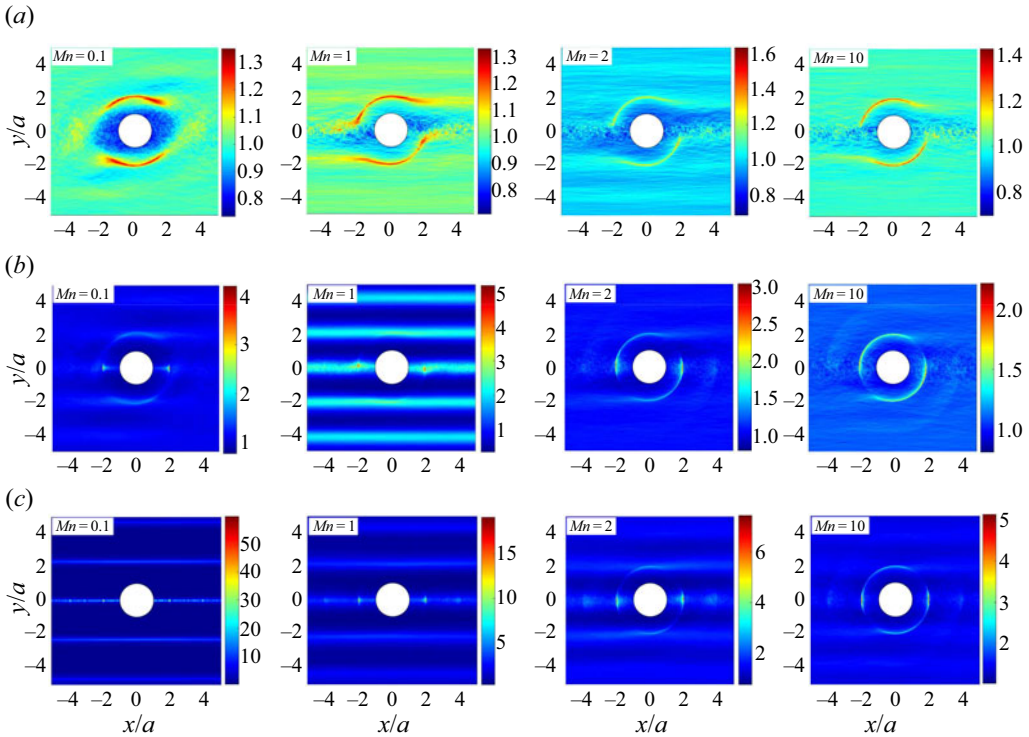


Figure 5. The projection of the pair distribution function onto the shear plane ( $x$ - $y$ ) at various Mason numbers: (a)  $\phi = 15\%$ ; (b)  $\phi = 30\%$ ; (c)  $\phi = 45\%$ .

suggests the strong negative normal stress in the  $y$  direction compared with the other two directions. This leads to the positive  $N_1$  and negative  $N_2$  at low Mason numbers ( $Mn < 1$ ), as seen in figures 4(a) and 4(b). On the other hand, for higher volume fractions of  $\phi \geq 30\%$ , the high probability at the equators corresponds to the strong negative normal stress in the  $x$  and  $z$  directions, leading to the negative  $N_1$  and positive  $N_2$  at low Mason numbers ( $Mn < 1$ ), as also seen in figures 4(a) and 4(b).

Increasing the shear rate then results in the notable distortion of the microstructure, as seen in figure 5 for  $Mn = 1, 2$  and  $10$ . At a low volume fraction of  $\phi = 15\%$  in figure 5(a), the microstructure evolves like a typical shear-driven suspension (Foss & Brady 2000), where the compressive and extensional axes are clearly identified. The anisotropy in the microstructure is further developed by increasing the Mason number. This microstructural anisotropy – the high probability along the compressional axis and the low probability along the extensional axis – indeed results in negative normal stress differences at high shear rates (Foss & Brady 2000; Sierou & Brady 2002; Cwalina & Wagner 2014). For a higher volume fraction of  $\phi = 30\%$  in figure 5(b), an intriguing microstructural feature is observed at  $Mn = 1$ , where a striped pattern or a string-like phase is horizontally formed in the direction perpendicular to the field ( $y$ ) direction. This observation suggests that the particles tend to assemble into two-dimensional ( $x$ - $z$ ) structures parallel to one another at a certain distance apart. This seemingly ordered microstructure could be responsible for a slight reduction in viscosity from  $Mn = 0.1$  to  $Mn = 1$  in figure 3(b), which could resemble shear thinning for hard-sphere colloidal suspensions (Phung, Brady & Bossis 1996; Wagner & Brady 2009). For a much higher

volume fraction of  $\phi = 45\%$  in [figure 5\(c\)](#), the horizontal striped patterns also emerge but form earlier at  $Mn < 1$  than for  $\phi = 30\%$ . A further increase in shear rate again leads to the microstructure being analogous to the typical shear-driven suspension for both  $\phi = 30\%$  and  $45\%$ , showing the anisotropic microstructure with respect to the compressive and extensional axes. Interestingly, the ordered patterns start to break around the critical Mason number ( $Mn = 1$ ), after which so-called hydroclusters are formed. A further rise in the viscosity during the shear-thickening process at  $\phi = 45\%$  compared with  $\phi = 30\%$  could be attributed to denser hydroclusters, which can be elucidated by the pair distribution functions at  $Mn = 10$  in [figures 5\(b\)](#) and [5\(c\)](#). Accompanying supplementary movies are available at <https://doi.org/10.1017/jfm.2023.980> and show the particle motions in a suspension for  $Mn = 0.1, 1$  and  $10$  at  $\phi = 30\%$  and  $45\%$ .

Here, we focus more on the stripped pattern observed in [figure 5\(b\)](#) at  $Mn = 1$  and [figure 5\(c\)](#) at  $Mn = 0.1$ . It is known that the particles tend to pair up briefly due to DIP or ICEP along the field ( $y$ ) direction and then immediately reorient towards the directions orthogonal to the field direction, after which they tend to repel from each other (Saintillan 2008; Park & Saintillan 2011a). Under sufficiently strong particle loading, specifically beyond the semidilute regime ( $\phi > 15\%$ ), we previously found that such pairing dynamics cause the particles to interact dominantly along the transverse directions ( $x, z$ ), resulting in the maximum probability of the pair distribution function at the particle equators (Mirfendereski & Park 2019), which is also seen in [figure 5](#). Upon the application of shear flow at which the shear effect is comparable to or weaker than the DIP effect, the particles tend to be trapped in the flow-vorticity ( $x$ – $z$ ) plane and thus self-assemble into two-dimensional horizontal sheets while still coherently moving in the flow ( $x$ ) direction. These two-dimensional sheet-like structures appear to experience no direct contact between them, making them move more easily (see accompanying supplementary movies for  $Mn = 1$  at  $\phi = 30\%$  and  $Mn = 0.1$  at  $\phi = 45\%$ ). Such a well-organized structural pattern under the flow is associated with less energy dissipation, resulting in a shear viscosity smaller than for the absence of the electric field, as seen in [figure 3\(b\)](#). However, these sheet-like structures are gradually disrupted by further increasing the Mason number, forming hydroclusters and, in turn, leading to the viscosity increase.

### 3.4. Suspension dynamics

We now attempt to illuminate the transition observed in the suspension rheology and microstructure around  $Mn = 1$  from a suspension dynamics point of view. A straightforward way to examine suspension dynamics is kinetics. We compute the contributions of DIP and shear to the r.m.s. velocity of particles, which are denoted as  $U_{rms}^{DIP}$  and  $U_{rms}^{Shear}$ , respectively. [Figure 6](#) presents the ratio of these two contributions,  $U_{rms}^{DIP}/U_{rms}^{Shear}$ , as a function of the Mason number for different volume fractions. The ratio seems to decrease almost linearly on the logarithmic scales with the Mason number. It passes the unity at  $Mn = 0.7$ – $1$ , around which there would be a changeover in the dominant mechanism of particle kinetics from DIP to shear dominance. Such a changeover could confirm the critical Mason number ( $Mn \approx 1$ ), which is identified by the relative shear viscosity in [figure 3\(b\)](#), the normal stress differences in [figure 4](#) and the microstructure in [figure 5](#). The inset of [figure 6](#) shows the changeover Mason number  $Mn_C$  as a function of volume fraction. There seems to be no general trend except in the range of  $Mn_C = 0.7$ – $1$ . Similar to the normal stress differences, large errors are observed at higher volume fractions due to stronger fluctuations. It is worth noting again that even small errors in the computation of each contribution of DIP and shear to the r.m.s. velocity can give rise

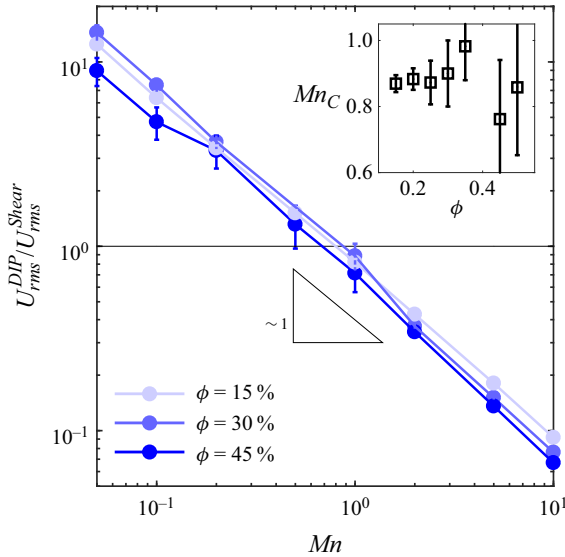


Figure 6. The ratio of the DIP contribution and the shear contribution to the root-mean-square (r.m.s.) velocity of particles ( $U_{rms}^{DIP} / U_{rms}^{Shear}$ ) as a function of Mason number on a log–log scale. Inset: the crossover Mason number  $Mn_c$  as a function of volume fraction. Note that the critical Mason number can be approximated when the ratio becomes unity,  $U_{rms}^{DIP} / U_{rms}^{Shear} = 1$ .

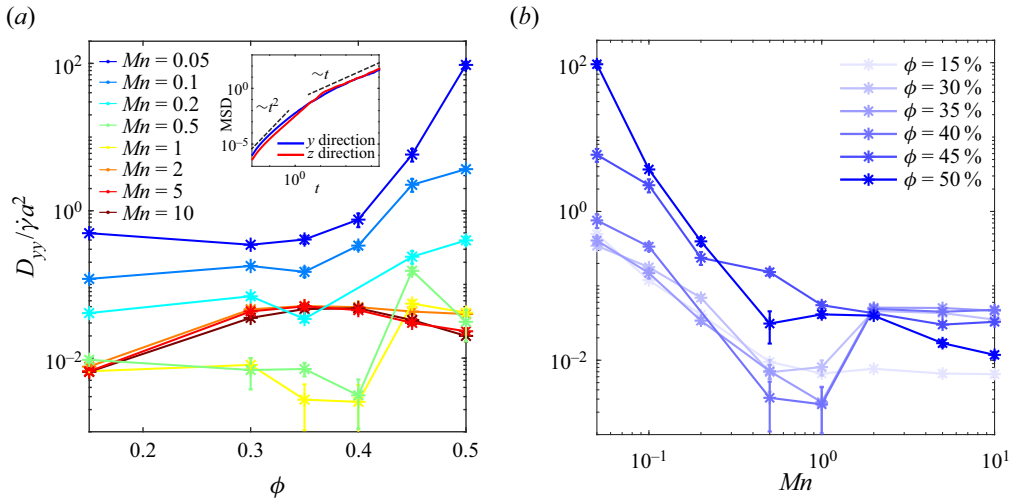


Figure 7. (a) Hydrodynamic diffusivity  $D_{yy}$  in the electric-field (y) direction, which is the same as the velocity-gradient direction of the external flow, as a function of volume fraction for a range of Mason numbers. Inset: the mean-square displacement (MSD) curves in the velocity-gradient (y) and vorticity (z) directions at  $\phi = 30\%$  and  $Mn = 0.05$ . (b) The diffusivity is replotted as a function of Mason number for various volume fractions.

to larger errors in the calculation of their ratio, which is also noted by Sierou & Brady (2002).

Finally, we investigate the hydrodynamic diffusion to make a further link between the suspension dynamics and the transition observed in the rheological properties and microstructure. To effectively quantify the hydrodynamic diffusion of a suspension, the MSD over time are calculated, as seen in the inset of figure 7(a) as an example in the

log–log plot. The MSD curve exhibits an initial quadratic growth with time followed by the diffusive regime with linear growth due to particle–particle interactions. The average slopes of the MSD curves over the diffusive regime give the effective hydrodynamic diffusivity tensor  $\mathbf{D}$  (Park & Saintillan 2010; Mirfendereski & Park 2019). Figure 7(a) shows the dependence of the diffusivity in the velocity-gradient direction  $D_{yy}$  on the volume fraction for various Mason numbers. Here  $D_{yy}$  also denotes the hydrodynamic diffusivity in the field direction. Note that the diffusivity  $D_{yy}$  is normalized by  $\dot{\gamma}a^2$ . At the smallest Mason number of  $Mn = 0.05$ , the diffusivity appears to be the largest across all volume fractions considered due to the strongest DIP interactions in comparison with other higher Mason numbers. At this Mason number, the diffusivity remains almost constant up to  $\phi \approx 35\%$ , after which it starts to increase with volume fraction. As the Mason number is increased, this trend seems to maintain up to  $Mn = 1$ , but its magnitude continues to decrease and reach a minimum at  $Mn = 1$ . Interestingly, as the Mason number is further increased, the diffusivity starts to increase, especially for  $20\% < \phi < 45\%$ . It then seems to collapse on a single curve for  $Mn \geq 5$  as it approaches the pure-shear-flow diffusivity, which is comparable with one observed by Sierou & Brady (2004). To more clearly demonstrate the transition around  $Mn = 1$ , the normalized diffusivity is replotted in figure 7(b) as a function of the Mason number for various volume fractions. As the Mason number increases, the diffusivity continues to decrease until  $Mn \approx 1$ , after which it becomes almost constant, except for  $\phi = 35\%$  and  $40\%$ , where there is a slight increase from  $Mn = 1$  to  $Mn = 2$ . Nevertheless, a clear transition is observed around  $Mn = 1$  in figure 7(b). Therefore, the suspension dynamics, characterized by the kinetics and hydrodynamic diffusion in figures 6 and 7, strongly supports a changeover in the dominant mechanism around the critical Mason number of  $Mn = 1$ , which ties closely into the transition observed in rheological properties and microstructure around  $Mn = 1$ .

#### 4. Conclusion

We have investigated for the first time the effects of DIP (the combination of two nonlinear electrokinetic phenomena – DEP and ICEP) on the shear rheology of suspensions of ideally conductive spheres using large-scale numerical simulations. For ideally conductive particles undergoing DIP in an electric field, the ICEP is known to be predominant over the DEP – thus the DEP effect is mostly neglected. To simulate the particle motions driven by both DIP and shear flow, we developed a simulation model that incorporates our previous model for DIP using the mobility-based Stokesian dynamics approach (Mirfendereski & Park 2019) combined with the classical resistance-based Stokesian dynamics approach (Brady & Bossis 1988) for shear flow in a periodic domain of the Lees–Edwards kind. The suspension is characterized by Mason number ( $Mn$ ), which is the ratio of viscous shear stress to electrokinetics-driven stress,  $Mn = \eta\dot{\gamma}/\varepsilon E_0^2$ . The suspension rheology was examined in a range of  $5 \times 10^{-2} \leq Mn \leq 10^2$  at volume fractions up to  $\phi = 50\%$ .

For shear viscosity, it was found that at high shear rates corresponding to high Mason numbers ( $Mn > 5$ ), the  $\phi$ -dependent shear viscosities collapse almost onto a single curve of a purely sheared suspension, demonstrating almost negligible effects of DIP. As the Mason number is decreased below  $Mn = 5$ , the  $\phi$ -dependent shear viscosity starts to decrease due to the increasing DIP effect, where a significant reduction of the viscosity is observed from  $Mn = 2$  to  $Mn = 1$ . As the Mason number is further decreased below  $Mn = 1$ , the viscosity slightly decreases as entering the low-shear-rate regime, where the  $\phi$ -dependent viscosity eventually collapses again onto another single curve for  $Mn < 0.5$ . For shear-dependent behaviours, it was found that the shear viscosity at a volume fraction



as small as  $\phi = 15\%$  is insensitive to a shear rate, showing Newtonian-like behaviour. For the semidilute regime at  $\phi \approx 30\%$ , the shear thickening starts to occur in which viscosity starts to sharply increase around  $Mn = 1$ . In the concentrated regime of  $\phi = 45\%–50\%$ , an almost five-fold increase in viscosity occurs during the shear thickening process. The microstructure was also investigated, where for low shear rates or DIP-dominant regimes  $Mn \leq 1$  and beyond semidilute regimes  $\phi \geq 30\%$ , the two-dimensional sheet-like structures are formed in the plane orthogonal to the velocity-gradient direction or electric-field direction. This structure helps a suspension flow easily, which is responsible for low viscosity. As a shear rate or the Mason number is increased above  $Mn \approx 1$ , such an organized structure is gradually disrupted, leading to the formation of the so-called hydroclusters, which eventually results in increasing viscosity and thus promoting the shear thickening.

For the normal stress differences, it was found that at low Mason numbers below  $Mn \approx 1$ , the first normal stress difference  $N_1$  is positive and the second normal stress difference  $N_2$  is negative at a low volume fraction of  $\phi = 15\%$ , implying that the effects of DIP on the normal stress differences are reminiscent of the Brownian contribution (Foss & Brady 2000). As a volume fraction is further increased for  $\phi \geq 30\%$ ,  $N_1$  and  $N_2$  show the opposite trend that  $N_1$  and  $N_2$  become negative and positive, respectively. This can be explained by the microstructure that exhibits the high probability of the pair distribution function in the flow and vorticity directions due to the effect of DIP, causing the particles to get trapped in two-dimensional sheets orthogonal to the velocity-gradient direction. For higher Mason numbers of  $Mn > 1$ , both  $N_1$  and  $N_2$  become negative across all volume fractions considered, and their magnitude increases with volume fraction.

To further illustrate the transition observed in rheological properties around  $Mn = 1$ , which we call the critical Mason number, suspension dynamics were investigated. The particle kinetics of each DIP and shear contribution were compared, showing that a changeover in the dominant kinetics is observed around  $Mn = 0.7–1$  from DIP to shear dominance. Furthermore, the hydrodynamic diffusivity in the velocity-gradient direction clearly exhibits the transition around  $Mn = 1$ . Its magnitude is the largest at the lowest Mason numbers  $Mn = 0.05$  due to the strong DIP effect and starts to decrease until reaching a minimum at  $Mn \approx 1$ , beyond which it becomes almost constant.

Lastly, the present study suggests the potential use of DIP or ICEP as a means to control the suspension rheology of conductive particles in an electric field. For instance, at high volume fractions (i.e.  $\phi \geq 30\%$ ) and high shear rates (i.e.  $Mn > 1$ ), having a stronger DIP effect via increasing the electric-field strength could reduce the viscosity from shear-thickened states. In addition, it also suggests that the direction or frequency of an electric field could play a promising role as a control parameter in controlling the rheology of such suspensions, allowing us to tune shear-thinning or shear-thickening behaviours. A detailed investigation of the active rheology control via an electric field for suspensions of conductive particles will be a subject of interesting future work.

**Supplementary movies.** Supplementary movies are available at <https://doi.org/10.1017/jfm.2023.980>.

**Acknowledgements.** This work was completed utilizing the Holland Computing Center of the University of Nebraska, which receives support from the Nebraska Research Initiative.

**Funding.** The authors gratefully acknowledge the financial support from the National Science Foundation through grants CBET-1936065 and CBET-2154788 and the Collaboration Initiative at the University of Nebraska.

**Declaration of interests.** The authors report no conflict of interest.

**Author ORCID*s*.**

 Siamak Mirfendereski <https://orcid.org/0000-0003-2918-0036>;

 Jae Sung Park <https://orcid.org/0000-0002-7966-1164>.

REFERENCES

- BATCHELOR, G.K. 1970 The stress system in a suspension of force-free particles. *J. Fluid Mech.* **41** (3), 545–570.
- BONNECAZE, R.T. & BRADY, J.F. 1992*a* Dynamic simulation of an electrorheological fluid. *J. Chem. Phys.* **96** (3), 2183–2202.
- BONNECAZE, R.T. & BRADY, J.F. 1992*b* Yield stresses in electrorheological fluids. *J. Rheol.* **36** (1), 73–115.
- BOSSIS, G. & BRADY, J.F. 1984 Dynamic simulation of sheared suspensions. I. General method. *J. Chem. Phys.* **80** (10), 5141–5154.
- BOSSIS, G. & BRADY, J.F. 1987 Self-diffusion of brownian particles in concentrated suspensions under shear. *J. Chem. Phys.* **87** (9), 5437–5448.
- BRADY, J.F. & BOSSIS, G. 1988 Stokesian dynamics. *Annu. Rev. Fluid Mech.* **20** (1), 111–157.
- BRADY, J.F. & MORRIS, J.F. 1997 Microstructure of strongly sheared suspensions and its impact on rheology and diffusion. *J. Fluid Mech.* **348**, 103–139.
- CHOI, S.B., CHEONG, C.C., JUNG, J.M. & CHOI, Y.T. 1997 Position control of an ER valve-cylinder system via neural network controller. *Mechatronics* **7** (1), 37–52.
- CHOI, S.B., HAN, Y.M., SONG, H.J., SOHN, J.W. & CHOI, H.J. 2007 Field test on vibration control of vehicle suspension system featuring ER shock absorbers. In *Electrorheological Fluids and Magnetorheological Suspensions*, pp. 496–503. World Scientific.
- CLARKE, A.S. & WILEY, J.D. 1987 Numerical simulation of the dense random packing of a binary mixture of hard spheres: amorphous metals. *Phys. Rev. B* **35** (14), 7350.
- CWALINA, C.D. & WAGNER, N.J. 2014 Material properties of the shear-thickened state in concentrated near hard-sphere colloidal dispersions. *J. Rheol.* **58** (4), 949–967.
- DAI, S.C., BERTEVAS, E., QI, F. & TANNER, R.I. 2013 Viscometric functions for noncolloidal sphere suspensions with Newtonian matrices. *J. Rheol.* **57** (2), 493–510.
- DAS, D. & SAINTILLAN, D. 2013 Electrohydrodynamic interaction of spherical particles under quince rotation. *Phys. Rev. E* **87**, 043014.
- DBOUK, T., LOBRY, L. & LEMAIRE, E. 2013 Normal stresses in concentrated non-Brownian suspensions. *J. Fluid Mech.* **715**, 239–272.
- DE VICENTE, J., KLINGENBERG, D.J. & HIDALGO-ALVAREZ, R. 2011 Magnetorheological fluids: a review. *Soft Matt.* **7** (8), 3701–3710.
- DENN, M.M., MORRIS, J.F. & BONN, D. 2018 Shear thickening in concentrated suspensions of smooth spheres in Newtonian suspending fluids. *Soft Matt.* **14** (2), 170–184.
- DOLINSKY, Y. & ELPERIN, T. 2009 Electrorotation of a leaky dielectric spheroid immersed in a viscous fluid. *Phys. Rev. E* **80**, 066607.
- DRISCOLL, M. & DELMOTTE, B. 2019 Leveraging collective effects in externally driven colloidal suspensions: experiments and simulations. *Curr. Opin. Colloid Interface Sci.* **40**, 42–57.
- DUKHIN, A.S. & MURTSOVKIN, V.A. 1986 Pair interaction of particles in electric field. 2. Influence of polarization of double layer of dielectric particles on their hydrodynamic interaction in a stationary electric field. *Colloid J. USSR* **48** (2), 203–209.
- DURLOFSKY, L., BRADY, J.F. & BOSSIS, G. 1987 Dynamic simulation of hydrodynamically interacting particles. *J. Fluid Mech.* **180**, 21–49.
- FENG, H., CHANG, H., ZHONG, X. & WONG, T.N. 2020 Recent advancement in induced-charge electrokinetic phenomena and their micro- and nano-fluidic applications. *Adv. Colloid Interface Sci.* **280**, 102159.
- FOLARANMI, G., TAU, M., BECHELANY, M., SISTAT, P., CRETIN, M. & ZAVISKA, F. 2022 Investigation of fine activated carbon as a viable flow electrode in capacitive deionization. *Desalination* **525**, 115500.
- FOSS, D.R. & BRADY, J.F. 2000 Structure, diffusion and rheology of brownian suspensions by Stokesian dynamics simulation. *J. Fluid Mech.* **407**, 167–200.
- GAMAYUNOV, N.I., MURTSOVKIN, V.A. & DUKHIN, A.S. 1986 Pair interaction of particles in electric field. 1. Features of hydrodynamic interaction of polarized particles. *Colloid J. USSR* **48** (2), 197–203.
- GUAZZELLI, É. & POULIQUEN, O. 2018 Rheology of dense granular suspensions. *J. Fluid Mech.* **852**, P1.
- HEIDARIAN, A., CHEUNG, S.C.P. & ROSENGARTEN, G. 2022 Slurry electrode properties for minimizing power loss of flowable electrochemical hydrogen storage systems. *Intl J. Hydrog. Energy* **47** (79), 33652–33663.

- JEFFREY, D.J. 1992 The calculation of the low Reynolds number resistance functions for two unequal spheres. *Phys. Fluids A* **4** (1), 16–29.
- JEFFREY, D.J. & ONISHI, Y. 1984 Calculation of the resistance and mobility functions for two unequal rigid spheres in low-Reynolds-number flow. *J. Fluid Mech.* **139**, 261–290.
- KHAIR, A.S. & BALU, B. 2019 The lift force on a charged sphere that translates and rotates in an electrolyte. *Electrophoresis* **40** (18–19), 2407–2414.
- KILIC, M.S. & BAZANT, M.Z. 2011 Induced-charge electrophoresis near a wall. *Electrophoresis* **32** (5), 614–628.
- KIM, S. & KARRILA, S.J. 2013 *Microhydrodynamics: Principles and Selected Applications*. Courier Corporation.
- KIM, S. & MIFFLIN, R.T. 1985 The resistance and mobility functions of two equal spheres in low-Reynolds-number flow. *Phys. Fluids* **28** (7), 2033–2045.
- KLINGENBERG, D.J., VAN SWOL, F. & ZUKOSKI, C.F. 1989 Dynamic simulation of electrorheological suspensions. *J. Chem. Phys.* **91** (12), 7888–7895.
- KLINGENBERG, D.J., VAN SWOL, F. & ZUKOSKI, C.F. 1991 The small shear rate response of electrorheological suspensions. II. Extension beyond the point-dipole limit. *J. Chem. Phys.* **94** (9), 6170–6178.
- LEES, A.W. & EDWARDS, S.F. 1972 The computer study of transport processes under extreme conditions. *J. Phys. C: Solid State Phys.* **5** (15), 1921–1928.
- LEWIS, T.B. & NIELSEN, L.E. 1968 Viscosity of dispersed and aggregated suspensions of spheres. *Trans. Soc. Rheol.* **12** (3), 421–443.
- LI, J., LIANG, X., LIOU, F. & PARK, J. 2018 Macro-/micro-controlled 3d lithium-ion batteries via additive manufacturing and electric field processing. *Sci. Rep.* **8** (1), 1–11.
- LOBRY, L. & LEMAIRE, E. 1999 Viscosity decrease induced by a DC electric field in a suspension. *J. Electrostat.* **47** (1), 61–69.
- MADEJA, J., KESY, Z. & KESY, A. 2011 Application of electrorheological fluid in a hydrodynamic clutch. *Smart Mater. Struct.* **20** (10), 105005.
- MARI, R., SETO, R., MORRIS, J.F. & DENN, M.M. 2014 Shear thickening, frictionless and frictional rheologies in non-Brownian suspensions. *J. Rheol.* **58** (6), 1693–1724.
- MARSHALL, L., ZUKOSKI, C.F. & GOODWIN, J.W. 1989 Effects of electric fields on the rheology of non-aqueous concentrated suspensions. *J. Chem. Soc. Faraday I* **85** (9), 2785–2795.
- MAZURSKY, A., KOO, J.H. & YANG, T.H. 2019 Design, modeling, and evaluation of a slim haptic actuator based on electrorheological fluid. *J. Intell. Mater. Syst. Struct.* **30** (17), 2521–2533.
- MELROSE, J.R. & HEYES, D.M. 1993 Simulations of electrorheological and particle mixture suspensions: agglomerate and layer structures. *J. Chem. Phys.* **98** (7), 5873–5886.
- MIRFENDERESKI, S. & PARK, J.S. 2019 Dipolophoresis in concentrated suspensions of ideally polarizable spheres. *J. Fluid Mech.* **875**, R3.
- MIRFENDERESKI, S. & PARK, J.S. 2021 The zero-shear-rate limiting rheological behaviors of ideally conductive particles suspended in concentrated dispersions under an electric field. *J. Rheol.* **65** (1), 13–26.
- MIRFENDERESKI, S. & PARK, J.S. 2022 Multiscale nature of electric-field-induced structural formations in non-colloidal suspensions. *Soft Matt.* **18** (36), 6916–6926.
- MURTSOVKIN, V.A. 1996 Nonlinear flows near polarized disperse particles. *Colloid J. Russ. Acad. Sci.* **58** (3), 341–349.
- NIKONENKO, V.V., KOVALENKO, A.V., URTE NOV, M.K., PISMENSKAYA, N.D., HAN, J., SISTAT, P. & POURCELLEY, G. 2014 Desalination at overlimiting currents: state-of-the-art and perspectives. *Desalination* **342**, 85–106.
- PAN, Z., DE CAGNY, H., WEBER, B. & BONN, D. 2015 S-shaped flow curves of shear thickening suspensions: direct observation of frictional rheology. *Phys. Rev. E* **92**, 032202.
- PANNACCI, N., LEMAIRE, E. & LOBRY, L. 2007 Rheology and structure of a suspension of particles subjected to quince rotation. *Rheol. Acta* **46** (7), 899–904.
- PARK, J.S. & SAINTILLAN, D. 2010 Dipolophoresis in large-scale suspensions of ideally polarizable spheres. *J. Fluid Mech.* **662**, 66–90.
- PARK, J.S. & SAINTILLAN, D. 2011a Electric-field-induced ordering and pattern formation in colloidal suspensions. *Phys. Rev. E* **83** (4), 041409.
- PARK, J.S. & SAINTILLAN, D. 2011b From diffusive motion to local aggregation: effect of surface contamination in dipolophoresis. *Soft Matt.* **7** (22), 10 720–10 727.
- PARTHASARATHY, M. & KLINGENBERG, D.J. 1996 Electrorheology: mechanisms and models. *Mater. Sci. Engng R Rep.* **17** (2), 57–103.

- VON PFEIL, K., GRAHAM, M.D., KLINGENBERG, D.J. & MORRIS, J.F. 2002 Pattern formation in flowing electrorheological fluids. *Phys. Rev. Lett.* **88** (18), 188301.
- PHUNG, T.N., BRADY, J.F. & BOSSIS, G. 1996 Stokesian dynamics simulation of Brownian suspensions. *J. Fluid Mech.* **313**, 181–207.
- PRADILLO, G.E., KARANI, H. & VLAHOVSKA, P.M. 2019 Quincke rotor dynamics in confinement: rolling and hovering. *Soft Matt.* **15**, 6564–6570.
- PRESSER, V., DENNISON, C.R., CAMPOS, J., KNEHR, K.W., KUMBUR, E.C. & GOGOTSI, Y. 2012 The electrochemical flow capacitor: a new concept for rapid energy storage and recovery. *Adv. Energy Mater.* **2** (7), 895–902.
- QIAN, B., MCKINLEY, G.H. & HOSOI, A.E. 2013 Structure evolution in electrorheological fluids flowing through microchannels. *Soft Matt.* **9**, 2889–2898.
- QUINCKE, G. 1896 Ueber rotationen im constanten electrischen felde. *Ann. Phys. Chem. Neue Folge Band* **59** (11), 417–485.
- RINTOUL, M.D. & TORQUATO, S. 1996 Computer simulations of dense hard-sphere systems. *J. Chem. Phys.* **105** (20), 9258–9265.
- ROMMERSKIRCHEN, A., GENDEL, Y. & WESSLING, M. 2015 Single module flow-electrode capacitive deionization for continuous water desalination. *Electrochem. Commun.* **60**, 34–37.
- RUIZ-LÓPEZ, J.A., FERNÁNDEZ-TOLEDANO, J.C., KLINGENBERG, D.J., HIDALGO-ALVAREZ, R. & DE VICENTE, J. 2016 Model magnetorheology: a direct comparative study between theories, particle-level simulations and experiments, in steady and dynamic oscillatory shear. *J. Rheol.* **60** (1), 61–74.
- SAAD, Y. & SCHULTZ, M.H. 1986 Gmres: a generalized minimal residual algorithm for solving nonsymmetric linear systems. *SIAM J. Sci. Stat. Comput.* **7** (3), 856–869.
- SAINTILLAN, D. 2008 Nonlinear interactions in electrophoresis of ideally polarizable particles. *Phys. Fluids* **20** (6), 067104.
- SAINTILLAN, D. 2018 Rheology of active fluids. *Annu. Rev. Fluid Mech.* **50**, 563–592.
- SAINTILLAN, D., DARVE, E. & SHAQFEH, E.S.G. 2005 A smooth particle-mesh Ewald algorithm for Stokes suspension simulations: the sedimentation of fibers. *Phys. Fluids* **17** (3), 033301.
- SÁNCHEZ-DÍEZ, E., VENTOSA, E., GUARNIERI, M., TROVÒ, A., FLOX, C., MARCILLA, R., SOAVI, F., MAZUR, P., ARANZABE, E. & FERRET, R. 2021 Redox flow batteries: status and perspective towards sustainable stationary energy storage. *J. Power Sources* **481**, 228804.
- SHENG, P. & WEN, W. 2012 Electrorheological fluids: mechanisms, dynamics, and microfluidics applications. *Annu. Rev. Fluid Mech.* **44**, 143–174.
- SHERMAN, Z.M. & SWAN, J.W. 2020 Spontaneous electrokinetic magnus effect. *Phys. Rev. Lett.* **124**, 208002.
- SHILOV, V.N. & SIMONOVA, T.S. 1981 Polarization of electric double-layer of disperse particles and dipolophoresis in a steady (DC) field. *Colloid J. USSR* **43** (1), 90–96.
- SIEROU, A. & BRADY, J.F. 2001 Accelerated Stokesian dynamics simulations. *J. Fluid Mech.* **448**, 115–146.
- SIEROU, A. & BRADY, J.F. 2002 Rheology and microstructure in concentrated noncolloidal suspensions. *J. Rheol.* **46** (5), 1031–1056.
- SIEROU, A. & BRADY, J.F. 2004 Shear-induced self-diffusion in non-colloidal suspensions. *J. Fluid Mech.* **506**, 285–314.
- SOLOVEICHIK, G.L. 2015 Flow batteries: current status and trends. *Chem. Rev.* **115** (20), 11533–11558.
- SQUIRES, T.M. & BAZANT, M.Z. 2004 Induced-charge electro-osmosis. *J. Fluid Mech.* **509**, 217–252.
- SQUIRES, T.M. & BAZANT, M.Z. 2006 Breaking symmetries in induced-charge electro-osmosis and electrophoresis. *J. Fluid Mech.* **560**, 65–101.
- STILLINGER, F.H. JR., DIMARZIO, E.A. & KORNEGAY, R.L. 1964 Systematic approach to explanation of the rigid disk phase transition. *J. Chem. Phys.* **40** (6), 1564–1576.
- TAN, H.W., AN, J., CHUA, C.K. & TRAN, T. 2019 Metallic nanoparticle inks for 3D printing of electronics. *Adv. Electron. Mater.* **5** (5), 1800831.
- VELEV, O.D. & BHATT, K.H. 2006 On-chip micromanipulation and assembly of colloidal particles by electric fields. *Soft Matt.* **2**, 738–750.
- WAGNER, N.J. & ACKERSON, B.J. 1992 Analysis of nonequilibrium structures of shearing colloidal suspensions. *J. Chem. Phys.* **97** (2), 1473–1483.
- WAGNER, N.J. & BRADY, J.F. 2009 Shear thickening in colloidal dispersions. *Phys. Today* **62** (10), 27–32.
- WANG, X.B., YANG, J., HUANG, Y., VYKOUKAL, J., BECKER, F.F. & GASCOYNE, P.R.C. 2000 Cell separation by dielectrophoretic field-flow-fractionation. *Anal. Chem.* **72** (4), 832–839.
- WHITTLE, M., BULLOUGH, W.A., PEEL, D.J. & FIROOZIAN, R. 1994 Dependence of electrorheological response on conductivity and polarization time. *Phys. Rev. E* **49**, 5249–5259.

*Rheology of conductive particles in electric field*

- XUAN, X. 2022 Review of nonlinear electrokinetic flows in insulator-based dielectrophoresis: from induced charge to Joule heating effects. *Electrophoresis* **43** (1–2), 167–189.
- YEH, S.R., SEUL, M. & SHRAIMAN, B.I. 1997 Assembly of ordered colloidal aggregates by electric-field-induced fluid flow. *Nature* **386** (6620), 57–59.
- ZARRAGA, I.E., HILL, D.A. & LEIGHTON, D.T.J. 2000 The characterization of the total stress of concentrated suspensions of noncolloidal spheres in Newtonian fluids. *J. Rheol.* **44** (2), 185–220.